AGU PUBLICATIONS

JGR

Journal of Geophysical Research: Space Physics

TECHNICAL REPORTS: METHODS

10.1002/2016JA022389

Special Section:
Measurement Techniques in Solar and Space Physics: Fields

Key Points:
- Atomic magnetometer for space has a total mass of less than 500 g and uses less than 1 W of power
- Miniaturization enabled by MEMS fabrication techniques and low-power semiconductor lasers
- Sensitivity of 15 pT/√Hz at 1 Hz is comparable to present state-of-the-art atomic magnetometers

Supporting Information:
- Supporting Information S1
- Data Set S1
- Data Set S2
- Data Set S3

Correspondence to:
H. Korth,
haje.korth@jhuapl.edu

Citation:
Korth, H., K. Strohbehn, F. Tejada, A. G. Andreou, J. Kitching, S. Knappe, S. J. Lehtonen, S. M. London, and M. Kafel (2016), Miniature atomic scalar magnetometer for space based on the rubidium isotope ^{87}Rb, *J. Geophys. Res. Space Physics*, *121*, 7870–7880, doi:10.1002/2016JA022389.

Received 14 JAN 2016
Accepted 11 JUL 2016
Accepted article online 23 JUL 2016
Published online 3 AUG 2016

©2016. The Authors.
This is an open access article under the terms of the Creative Commons Attribution-NonCommercial-NoDerivs License, which permits use and distribution in any medium, provided the original work is properly cited, the use is non-commercial and no modifications or adaptations are made.

Miniature atomic scalar magnetometer for space based on the rubidium isotope ^{87}Rb

Haje Korth[1], Kim Strohbehn[1], Francisco Tejada[2], Andreas G. Andreou[2], John Kitching[3], Svenja Knappe[3], S. John Lehtonen[1], Shaughn M. London[1], and Matiwos Kafel[1]

[1]The Johns Hopkins University Applied Physics Laboratory, Laurel, Maryland, USA, [2]Electrical and Computer Engineering, The Johns Hopkins University, Baltimore, Maryland, USA, [3]National Institute of Standards and Technology, Boulder, Colorado, USA

Abstract A miniature atomic scalar magnetometer based on the rubidium isotope ^{87}Rb was developed for operation in space. The instrument design implements both M_x and M_z mode operation and leverages a novel microelectromechanical system (MEMS) fabricated vapor cell and a custom silicon-on-sapphire (SOS) complementary metal-oxide-semiconductor (CMOS) integrated circuit. The vapor cell has a volume of only 1 mm^3 so that it can be efficiently heated to its operating temperature by a specially designed, low-magnetic-field-generating resistive heater implemented in multiple metal layers of the transparent sapphire substrate of the SOS-CMOS chips. The SOS-CMOS chip also hosts the Helmholtz coil and associated circuitry to stimulate the magnetically sensitive atomic resonance and temperature sensors. The prototype instrument has a total mass of fewer than 500 g and uses less than 1 W of power, while maintaining a sensitivity of 15 pT/√Hz at 1 Hz, comparable to present state-of-the-art absolute magnetometers.

1. Introduction

The magnetic field is a fundamental physical quantity, and its precise measurement plays a central role in addressing the scientific objectives of many planetary, solar, and interplanetary science missions. Magnetic fields in space have been measured by fluxgate magnetometers [e.g., *Smith et al.*, 1998; *Anderson et al.*, 2007], proton-precession magnetometers [e.g., *Duret et al.*, 1995; *Reigber et al.*, 2002], and optically pumped magnetometers [e.g., *Smith et al.*, 1975; *Dougherty et al.*, 2004; *Leger et al.*, 2009]. A review of space-based magnetometers can be found in *Acuña* [2002]. Of these instruments, fluxgate magnetometers are the most widely used because they measure the vector magnetic field with good sensitivity and require only modest mass and power resources. Because fluxgate magnetometers measure voltages proportional to the ambient magnetic field, their scale factors and offsets must be calibrated and are subject to drift over time and temperature. On the other hand, the measurement technique of proton precession and optically pumped magnetometers is based on fundamental physical quantities such as the magnetic moment and spin angular momentum of electrons and atomic nuclei. While the operating principle of proton-precession magnetometers is based on nuclear magnetic resonance, optically pumped magnetometers are based on the precession of electron spins as the mechanism for magnetic field detection. Both types of atomic magnetometers have demonstrated excellent performance with respect to sensitivity (10 to 50 pT root-mean-square (RMS)), absolute accuracy (0.1 to 1.0 nT), and dynamic range (1000 to 100,000 nT) [*Duret et al.*, 1995; *Dougherty et al.*, 2004; *Leger et al.*, 2009] while providing long-term absolute accuracy and stability. However, a major disadvantage of these instruments is their significant mass and high-power requirements. With sensor volumes as large as several hundred cubic centimeters, these instruments can draw more than 10 W of power and can have a mass of several kilograms. In addition, because the atomic resonances sensed by these instruments do not provide directional magnetic field information, vector measurement capability, which is required by most space-based scientific missions, must either be retrofitted or obtained in combination with a fluxgate magnetometer. These disadvantages effectively prevent the routine application of atomic magnetometers in space. Hence, reductions in mass, size, and power consumption of these instruments substantially enhance the potential for more widespread use of atomic magnetometers in space.

In response to an ongoing paradigm shift in space research to reduce launch cost by employing smaller, highly integrated technologies, we have developed a low-resource, miniaturized atomic scalar magnetometer based on optically pumped rubidium. Our instrument takes advantage of recent breakthroughs in microfabricated atomic devices [*Schwindt et al.*, 2004, 2007], which have demonstrated reductions of power

requirements and mass by 1 to 2 orders of magnitude over conventional instruments. The resulting instrument has a total mass of fewer than 500 g and uses less than 1 W of power, while maintaining a sensitivity of 15 pT/√Hz at 1 Hz, comparable to present state-of-the-art absolute magnetometers. The instrument employs two complementary but independent measurement techniques, and the magnetic field estimates obtained from these techniques agree to within 2 nT.

The technology we have developed is an atomic magnetometer based on the rubidium isotope ^{87}Rb. Atomic magnetometers infer the magnetic field from the Larmor precession of atomic spins, whereby the associated Larmor frequency, $f[\mathrm{Hz}] = \gamma B/2\pi$, to lowest order in magnetic field strength, B, is proportional to B and to the gyromagnetic ratio, $\gamma/2\pi$. For ^{87}Rb, the gyromagnetic ratio is $\gamma/2\pi = 7$ Hz/nT. Atomic magnetometers have recently become competitive with [*Kominis et al.*, 2003] the sensitivity of the traditional "gold standard" of magnetometers based on superconducting quantum interference devices [e.g., *Jaklevic et al.*, 1964; *Drung et al.*, 2007]. These advances have been enabled by the combination of highly sensitive optical detection based on polarization rotation and the suppression of line broadening due to spin-exchange collisions between alkali atoms. There has been simultaneous work to reduce the size of these types of atomic magnetometers using microelectromechanical system (MEMS) microfabrication techniques [*Schwindt et al.*, 2004, 2007]. Recent work combining these principles has demonstrated that a sensitivity below 10 pT/√Hz can be achieved at field strengths observed at the Earth's surface [*Schwindt et al.*, 2004] and that the sensitivity can be improved below 100 fT/√Hz at low magnetic fields in a detection volume of 6 mm^3 [*Shah et al.*, 2007; *Mhaskar et al.*, 2012].

Traditionally, alkali atom magnetometers have not been strong candidates for high-accuracy applications due in part to the presence of the nonlinear Zeeman shift caused by the net magnetic moment of the atomic nucleus [*Back and Goudsmit*, 1928]. This effect results in shifts of the Larmor precession frequency that depend on the direction of the external field with respect to the axis of symmetry of the magnetometer sensor. The error in the derived magnetic field magnitude depends on the type of alkali atom and on the line width of the magnetic resonance. The nonlinear Zeeman effect is not present in ^{4}He or proton magnetometers because ^{4}He has no nuclear spin, and the operating principle of proton magnetometers is based on the precession of the polarized nucleus itself. However, these highly accurate magnetometers have not been miniaturized at a level that would allow for widespread application in space, where power is scarce and small size and mass is critical. Developing a ^{4}He magnetometer that is not only small but that can operate on less than 1 W of power is problematic from several viewpoints, including the need for a radio-frequency (RF) discharge to access the magnetically sensitive metastable atomic level and the unavailability of suitable low-power, $<$10 mW, excitation lasers. Fortunately, the nonlinear Zeeman shift only represents a significant source of error in alkali magnetometers at a magnetic field strength above 10,000 nT [*Schwindt et al.*, 2007], and many applications involve magnetic fields much lower than this.

Below we describe the development of a miniature atomic scalar magnetometer, which was a collaborative project between the Johns Hopkins University Applied Physics Laboratory, Johns Hopkins University Whiting School of Engineering, and the National Institute of Standards and Technology. The particular focus of the effort presented here are (1) development of a small-scale magnetic field sensor based on a microfabricated ^{87}Rb vapor cell and custom ultralow-field heaters, (2) qualification of the sensor for space flight by subjecting the sensor optical components to radiation testing and by performing a structural analysis of the sensor assembly, (3) development of signal-processing electronics to sense and track the Larmor frequency to provide a continuous time series of magnetic field measurements, and (4) testing of the prototype magnetometer to assess its sensitivity. The operating principle and hardware description of the optically pumped magnetometer are provided in section 2. Analysis of the instrument performance is presented in section 3, and the results are summarized in section 4.

2. Hardware Description

2.1. Operating Principle of Optically Pumped Magnetometers

Most atomic optically pumped magnetometers are based on the Larmor precession of electron or nuclear spins in a magnetic field [e.g., *Colegrove and Franken*, 1960; *Bloom*, 1962]. Briefly, a cell containing a suitable gas is illuminated with circularly polarized light with a wavelength that corresponds to resonance with an optical (electronic) transition in the atoms. Under these conditions, atoms are optically pumped into a

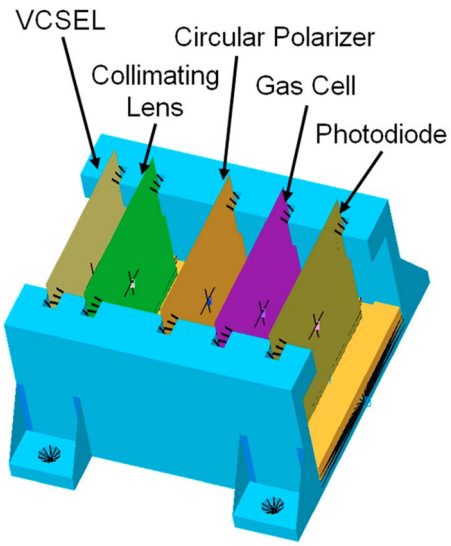

Figure 1. Miniature atomic scalar magnetometer configuration.

nonthermal population distribution, and the vapor cell becomes largely transparent to the optical beam. If the cell is then subjected to an RF signal at the Larmor precession frequency, an oscillating population distribution is excited within the atoms, which causes a time-dependent modulation of the optical transmission. By detecting the phase shift or amplitude variation of the atomic response, the Larmor frequency can be determined, and, from that, the magnetic field magnitude can be deduced. The most commonly used elements for optically pumped magnetometers are metastable helium and alkali metals like cesium, rubidium, and potassium.

Optically pumped magnetometers operate on one of the several modes linked to the atomic spin system. The behavior of the atomic spin system can be described by three variables M_x, M_y, and M_z of Bloch's equations for a spin system [*Bloch*, 1946]. Helium magnetometers, designed for high accuracy, commonly operate in the M_z mode, giving rise to a secular change in light intensity as a function of the frequency of the drive field, which reaches a minimum when the RF field oscillates at the Larmor frequency and the vapor cell becomes opaque. In contrast, alkali metal magnetometers, designed for high sensitivity, typically employ the M_x mode, manifested as a high-frequency light modulation synchronized with the driving RF field [*Bloom*, 1962]. The corresponding resonant signal is shifted in phase relative to that of the RF field, and at the Larmor frequency, this phase shift amounts to 90°. The miniature rubidium magnetometer described here selectively uses M_x or M_z mode magnetic field detection.

The sensitivity of optically pumped magnetometers is a function of the angle θ between the sensor's optical axis and the magnetic field direction and varies for the M_x mode as $\sin(\theta)\cos(\theta)$ and for the M_z mode as $\cos^2(\theta)$ [*Bloom*, 1962]. It thus peaks for angles of 45° and 0° in M_x and M_z mode, respectively. In contrast, the sensor is insensitive for magnetic field orientations of 0° and 90° in M_x mode and of 90° in M_z mode; these are the so-called polar (0°) and equatorial (90°) dead zones. Because the equatorial dead zone is common to both the M_x and M_z modes, a single sensor does not support omnidirectional measurements. To provide observations for arbitrary magnetic field directions, multiple sensors must ultimately be used and configured appropriately. Such demonstration is beyond the scope of this work.

2.2. Sensor Hardware

Taking advantage of recent advances in technology, we have developed a device that has potential to become a next-generation miniature, low-resource, high-precision, high-sensitivity, space-qualified absolute scalar magnetometer. The technology is based on a low-power semiconductor laser and a miniature rubidium vapor cell of millimeter dimensions produced using modern microfabrication processes [*Liew et al.*, 2004, 2007]. These MEMS vapor cells have been used as frequency references in atomic clocks [*Knappe et al.*, 2005a, 2005b], but they also have been shown to function as sensitive magnetometers [*Schwindt et al.*, 2004, 2007]. The combination of MEMS vapor cell and a carefully stabilized semiconductor diode laser has allowed a substantial reduction in mass, size, and power dissipation of both clocks and magnetometers, with only modest decrease in performance. The MEMS vapor cell has been integrated into a magnetic field sensor configured as shown in Figure 1. The microfabricated rubidium vapor cell is illuminated by light emitted from a vertical-cavity surface-emitting laser (VCSEL) at a nominal wavelength of 795 nm, corresponding to a frequency of about 377 THz. The laser light passes through an optic package, where the laser light is collimated and circularly polarized. The resonant response of the atoms is detected using a discrete photodiode. The sensor supports both M_x and M_z mode operations. The assembled

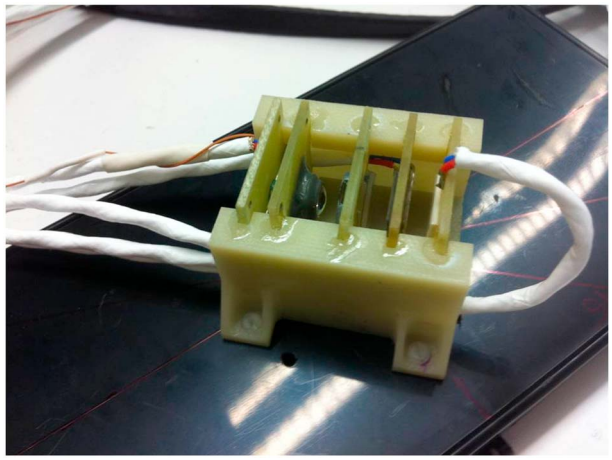

Figure 2. Assembled miniature atomic scalar magnetometer sensor.

prototype sensor, shown in Figure 2, measures $35 \times 25 \times 25\,\mathrm{mm}^3$ and has a mass of 44 g. Future reductions in size and mass are anticipated and have already been demonstrated in sensors not intended specifically for use in space [*Schwindt et al.*, 2004, 2007; *Mhaskar et al.*, 2012].

An additional key component in the miniaturization of the device is the monolithic integration of the vapor gas chamber with heaters, temperature sensors, and Helmholtz coils on a silicon-on-sapphire (SOS) complementary metal-oxide-semiconductor (CMOS) chip. The SOS-CMOS process has a feature size of 500 nm realized within a 100 nm ultrathin silicon (UTSi) active layer atop a sapphire substrate. There are three metal interconnection layers and one polysilicon layer. The SOS-CMOS process [*Andreou et al.*, 2001; *Andreou*, 2008] offers a number of advantages over more standard processes, including optical transparency, lower power, higher speed, and radiation hardness. In addition, the UTSi SOS technology provides devices with lower parasitic capacitances than standard CMOS technologies and offers the designer three threshold variations for both *p* type and *n* type metal-oxide-semiconductor field-effect transistors, as compared to the two types typically available in most bulk CMOS technologies. The fully depleted devices with their multiple thresholds, higher normalized transconductance, and reduced parasitics yield high-performance analog blocks. However, besides optical transparency, the most important consideration of using SOS-CMOS as the transparent faceplates with the built-in heaters is the high thermal conductivity of the sapphire substrate. A high value of thermal conductivity facilitates the uniform heating of the Rb gas in the chamber underneath.

The SOS-CMOS devices are mounted to the two faces of the vapor cell perpendicular to the optical axis. The SOS-CMOS technology was chosen because the sapphire substrate is intrinsically transparent to the light emitted at the wavelength of the laser. The functionality of the SOS-CMOS chips, the layout of which is shown in Figure 3, is threefold. First, they host a resistive heater at its center, which heats the vapor cell to it operating temperature of about 100°C using 0.5 W of power generated by a 10 mA current from a 50 V power supply. Even though the heater current is low, extreme care must be taken in the implementation of the heater

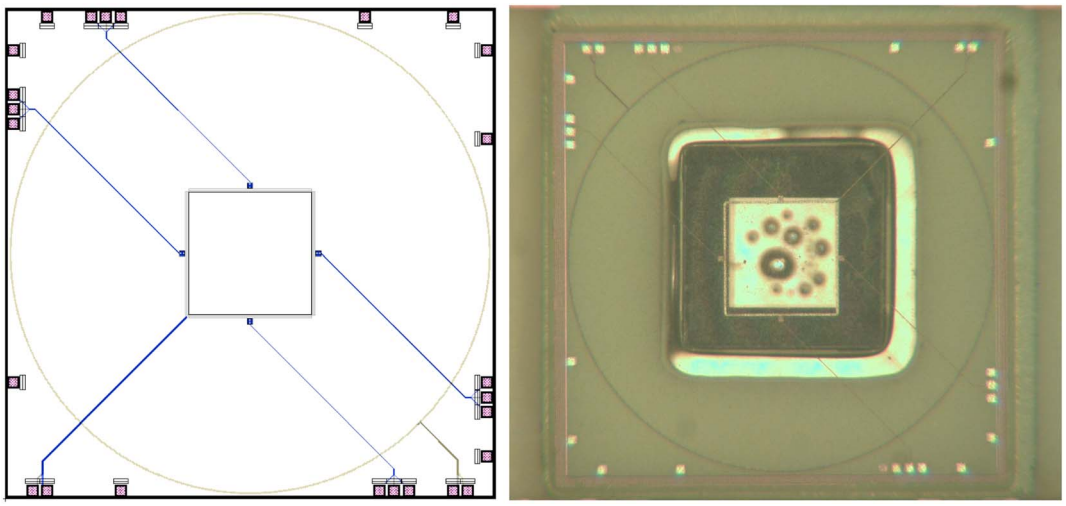

Figure 3. SOS-CMOS (left) layout and (right) photo showing the double compensated square-loop heater and attached temperature sensors at the center and a circular coil for RF excitation near the edge.

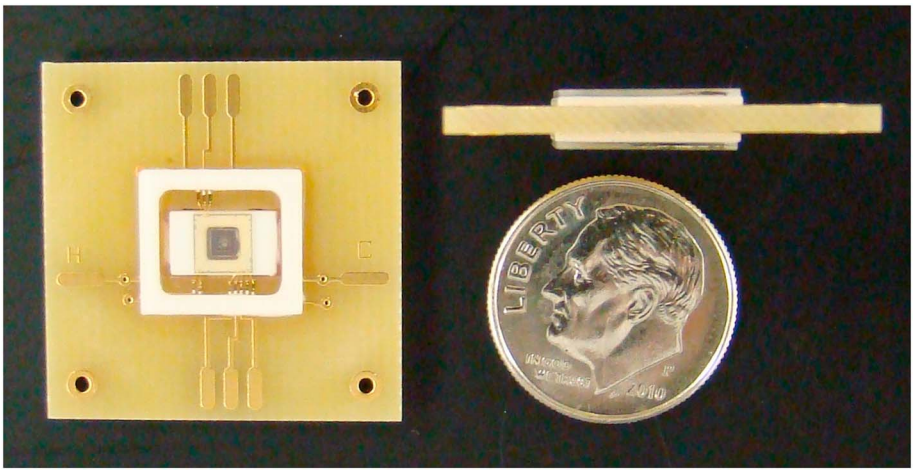

Figure 4. Front and side view of the vapor cell assembly including the transparent SOS-CMOS dies.

because the flow of current generates an undesirable magnetic field in close vicinity of the detection volume. To minimize interference with the measurement of the ambient field, the integrated conductor widths and spacing on the 0.5 μm SOS-CMOS chip are on micrometer scales, and near-perfect magnetic compensation was achieved using two sets of dual square loops arranged in neighboring conducting layers of the chip. The stray magnetic field due to the heater at the location of the cell was measured to be less than 10 nT, and comparison with numerical calculations shows that the finite residual field is largely due to limitations in the accuracy of the alignment of the two SOS-CMOS dies. The magnetic field per unit current generated by the heater is readily obtained by measuring the field at two distinct heater current levels. The measurements can thus be corrected for this contribution to within the knowledge of the heater current, 0.5 mA, corresponding to 0.5 nT. In the future, the contributions of the heater to the magnetic field measurement may be eliminated by operating the heater with an AC current at a frequency far outside the bandwidth of the instrument. The second function of the SOS-CMOS die is to generate the RF magnetic field necessary to establish the atomic resonance via a single-turn circular coil. To maximize the uniformity of this field across the detection volume, the coils of both SOS-CMOS dies are sized to yield the Helmholtz arrangement, where the coil radius matches their separation prescribed by the thickness of the vapor cell. Finally, the SOS-CMOS die includes temperature-sensing diodes for regulation of the vapor-cell temperature and circuitry for signal conditioning. The system reported in this paper does not yet use the latter electronic circuits. Instead, this functionality is implemented externally to the sensor in the main electronics. The assembled vapor cell including transparent SOS-CMOS dies is shown in Figure 4. Even though this design employs SOS-CMOS, future designs can also employ more advanced silicon-on-insulator (SOI) CMOS technology [*Tejada et al.*, 2006] with the silicon substrate appropriately micromachined to allow light through the system. The SOI substrate reduces the parasitic device capacitance and thereby improves performance, which can be beneficial if signal processing within the sensor is found to be viable in the future.

The ability of the magnetometer components to operate under conditions of prolonged exposure to radiation in a space environment has been tested. The active and passive sensor optical components (Figure 1) have been exposed to high-energy proton radiation with a maximum total dose of 50 krad (Si). The findings from the exposure tests are that (1) the transparency of the components did not show changes greater than the 3% uncertainty in the measurements; (2) the VCSEL output power decreased on average by 2% and can be compensated by adjusting the laser current and temperature accordingly within the designed control ranges of the electronics to keep the wavelength tuned to the atomic resonance; (3) the photodiode sensitivity decreased on average by 14%, which should cause no first-order change in the magnetometer reading because the field magnitude is deduced from a frequency measurement; and (4) while the photodiode dark current increased after exposure by a factor of 40, the maximum dark current observed among the exposed components was about 2 orders of magnitude lower than the photocurrent modulation induced by the Larmor precession. Subsequent exposure to γ-radiation of equal total dose did not yield further measurable degradation of the optical components.

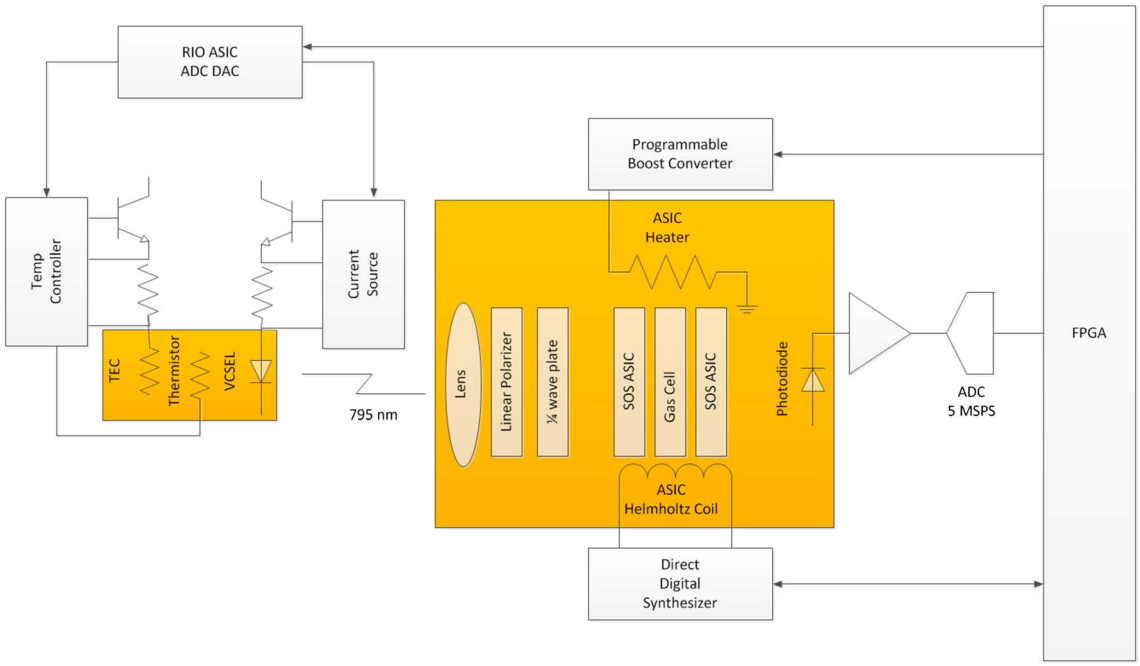

Figure 5. Signal-processing block diagram. The orange boxes indicate the components contained within the sensor.

The selection of the sensor's optical components was based on earlier development efforts by *Schwindt et al.* [2007]. While these parts successfully passed radiation testing to a modest total dose, they were not specifically designed to be radiation tolerant. It is quite possible that components offering better performance after prolonged exposure to radiation exist. For example, the photodiodes integrated on the SOS-CMOS (but not used in this setup) were characterized for radiation exposure with good results [*Marwick et al.*, 2006]. We intend to revisit the part selection for application-specific environments in the future. In the meantime, the technology can be adapted for operation in higher-radiation space environments using appropriate shielding [*Podzolko et al.*, 2009].

A finite element structural analysis was carried out to assess the ability of the sensor to withstand vibration forces exerted on the sensor during a rocket launch. The constrained modal analysis of the sensor showed that the first-mode frequency of the model sensor was 4100 Hz. Since this frequency well exceeds the 2000 Hz upper limit of concern for launch operations, random vibration testing was not performed and a static loading analysis was performed instead. The latter analysis indicated that even under severe static loading conditions of 150 g, where $g = 9.81\ \mathrm{m\,s^{-2}}$ is the Earth's gravitational acceleration, imposed along any axis of the sensor, displacement of individual sensor components is less than 2.5×10^{-5} m with positive safety margins. The results from the structural analysis indicate that the sensor technology is capable of enduring launch conditions.

2.3. Control Electronics

The sensor is controlled digitally by a field-programmable gate array (FPGA), which generates the signal to excite the rubidium atoms within the vapor cell and measures and processes the resonant response. In addition, the FPGA implements the Larmor frequency tracking loop and provides an interface to a host laptop computer (running MATLAB for convenience). The sensor operation is illustrated in the control electronic block diagram in Figure 5, in which orange boxes indicate the components contained within the sensor. Light from the VCSEL is collimated by a lens, circularly polarized, passed through the vapor cell, and finally detected with a silicon photodiode. A transimpedance amplifier converts the photocurrent to a voltage, which is digitized to 12 bits at 5 Msamples per second and read by the FPGA. This digitized photocurrent signal contains all the sensor information. The prototype signal-processing electronics is implemented on a $15 \times 10\ \mathrm{cm}^2$ printed circuit board using flight-equivalent electrical components. The mass of the electronics is 440 g, but the layout is not yet optimized to minimize resources.

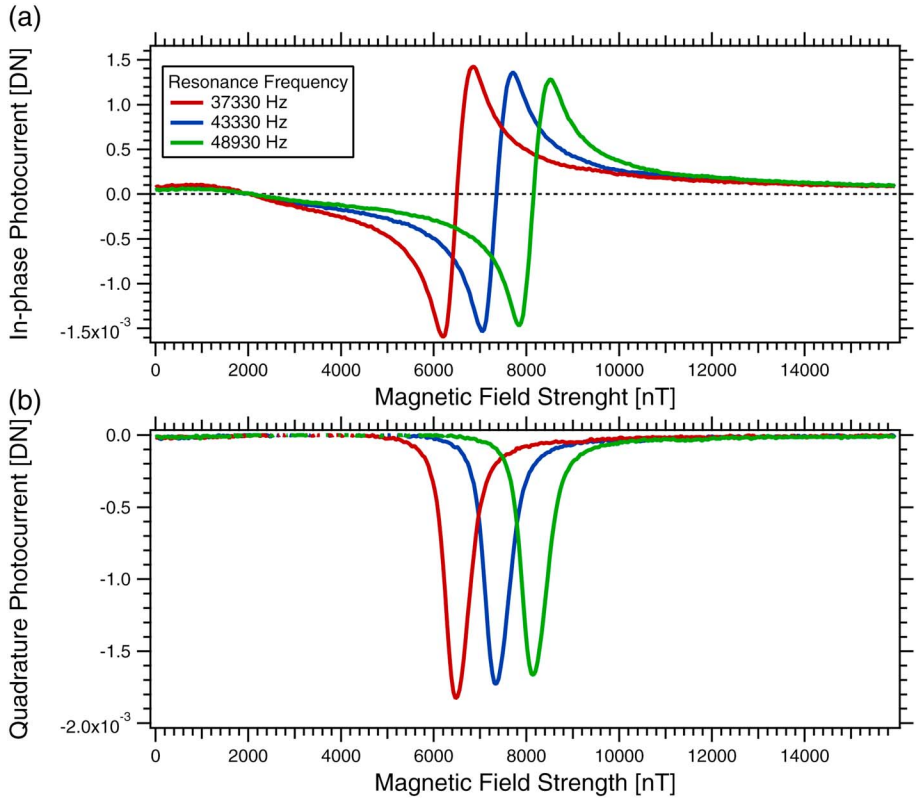

Figure 6. (a) In-phase and (b) quadrature components of the photocurrent as function of the ambient magnetic field strength for three fixed RF resonance frequencies applied via the Helmholtz coils.

To stimulate atomic resonances, the rubidium vapor density must be sufficiently high, and, in most environments, the vapor cell must be heated to increase the vapor pressure and thus the number of atoms in the gaseous state. The FPGA controls the vapor-cell temperature by adjusting a pulse width modulated (PWM) signal provided to the heater boost converter. A higher heater voltage results in more heater current and thus a warmer vapor cell. The precise temperature of the vapor cell is not extremely critical. It must be hot enough for the rubidium to evaporate but not so hot as to cause line broadening from spin-exchange collisions. This level of control is easily achieved by 8 bits of PWM control and reading the temperature-sensing diode on the SOS-CMOS die with a voltage-to-frequency converter. The vapor-cell temperature is typically regulated to approximately 100°C.

To excite the atomic resonance, the VCSEL is tuned to the D1 line of ^{87}Rb at 795 nm. The wavelength of the VCSEL is controlled by both current and temperature and is regulated as follows. The FPGA controls a programmable VCSEL drive current source by means of a custom mixed-signal application-specific integrated circuit, which was developed for use in space-flight instrumentation at the Johns Hopkins University Applied Physics Laboratory [*Martin and Meitzler*, 2012]. The VCSEL current is adjusted to provide approximately full-scale digital output when the vapor cell is not heated. With the current drive commanded to this level, the VCSEL temperature is swept slowly to modify the wavelength until the digitized light level reaches a minimum at the center of the 795 nm absorption line. The VCSEL temperature corresponding to the minimum signal is selected as the temperature set point, which is used by the FPGA to command the temperature controller. The temperature set point does not have to be adjusted again unless the VCSEL drive current is changed.

To infer the ambient magnetic field magnitude, the FPGA controls a direct digital synthesis (DDS) circuit with 32-bit, 0.23 mHz frequency resolution to excite the Helmholtz coils hosted on the SOS-CMOS dies. As described earlier, the digitized photodiode signal is modulated at the Helmholtz drive frequency and exhibits a maximum amplitude and 90° phase shift when the Helmholtz coil drive frequency is equal to the Larmor frequency. This modulated signal is typically quite small, so we implemented a digital lock-in amplifier in

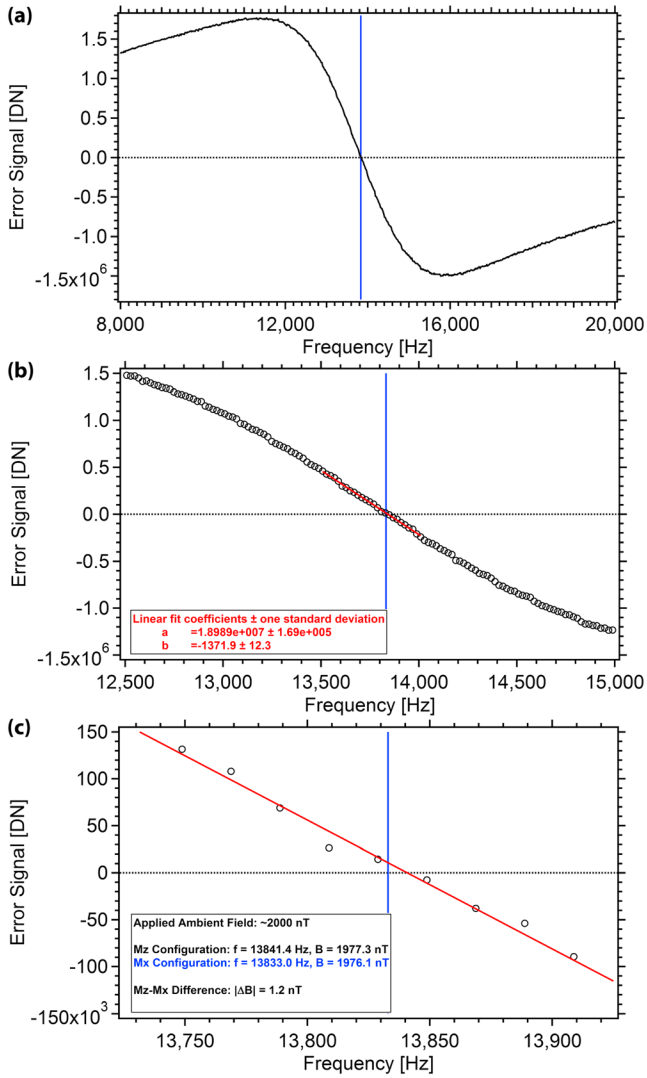

Figure 7. M_z error signal versus frequency measured for an ~2000 nT ambient field. (a–c) The measurements in decreasing frequency ranges spanning the resonant frequency, f_0. The red line represents a linear fit of the data within the interval [13,500; 14,000] Hz. The fit parameters are indicated in Figure 7b, and the magnetic field magnitude corresponding to f_0 is compared to that obtained in M_x operation (vertical blue line) in Figure 7c.

the FPGA. The lock-in uses the sensed DDS drive as an in-phase reference and performs digital phase shifting to generate a quadrature reference. The narrowband lock-in operation produces in-phase and quadrature signals, which are integrated over many cycles of the Larmor frequency. As shown in Figure 6, the in-phase signal minimizes at the Larmor frequency and the absolute value of the quadrature signal is maximized for M_x operation.

The photodiode signal is similarly too noisy for direct detection of the resonant frequency, f_0, in M_z mode. Instead, the lock-in amplifier detects the light transmission, A, at frequencies $f_1 = f - \Delta f$ and $f_2 = f + \Delta f$, and an error signal, $\Delta A = A(f_1) - A(f_2)$, is computed from the difference. A symmetric absorption line implies $\Delta A = 0$ at $f = f_0$. The M_z mode control loop outputs data at a rate of 5 samples per second. Figure 7 shows the error signal as a function of frequency for an ambient field of ~2000 nT on three different frequency scales, decreasing in width from top to bottom. As seen in the figure, the function $\Delta A(f)$ is overall dispersive but approximately linear near f_0. The transition of the error signal through zero was evaluated from linear fitting of the ΔA measurements within a 500 Hz frequency range approximately centered on the Larmor frequency. The fit result is indicated by red lines in Figures 7b and 7c and yields a resonant frequency of 13,841.4 Hz, corresponding to a magnetic field magnitude of 1977.3 nT. The experiment was repeated using M_x mode, which measured a frequency of 13,833.0 Hz, corresponding to 1976.1 nT, represented by the vertical blue lines in Figure 7. The measurements obtained in the M_x and M_z modes agree closely to within 1.2 nT but are not identical. The origin of the discrepancy remains under investigation but could be due to misalignment of the optical axis with the RF coil axis and/or spurious phase shifts in the M_x signal; both of which are sources of reading errors in M_x magnetometers. We note that the discrepancy is smaller than offset drifts sometimes experienced by fluxgate magnetometers due to variations in the thermal environment. While the M_z mode is, at least in theory, more accurate, it is also an order of magnitude slower than the M_x mode because the electronics has to average the M_z signal response over several cycles.

Continuous magnetic field measurements are obtained by tracking the Larmor frequency as follows: initially, the frequency of the current driving the Helmholtz coils is slowly swept from 500 kHz down to 700 Hz, corresponding to magnetic field magnitudes of 71,428 and 100 nT, respectively, in 100 Hz steps. For each step, the

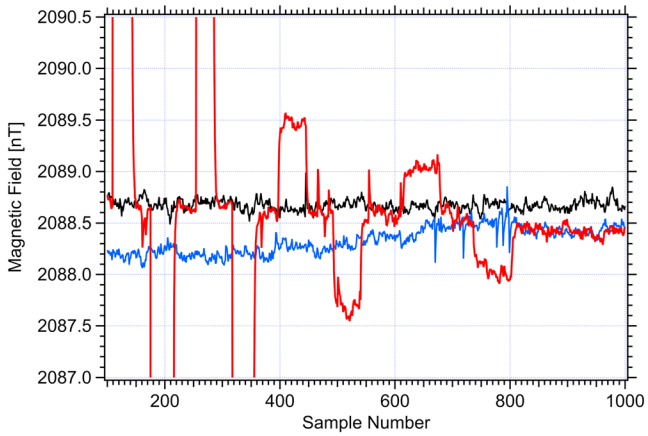

Figure 8. Magnetic field magnitude measured in M_x mode versus sample number for step-like changes of the magnetic field applied via a solenoid (red line) and for two independent time series of a quiet ambient field inside a six-layer set of mu-metal cans (black and blue lines).

absolute value of the quadrature signal is compared to an acquisition threshold. When the quadrature absolute value is above threshold, the Larmor track loop uses the in-phase signal as an error signal to digitally servo the DDS to null the in-phase signal at the Larmor frequency. The Larmor frequency is then determined by the commanded 32-bit DDS command word. The sign of the error signal is determined from the sign of the quadrature signal, since these signals can invert for changes in field geometry. The tracking loop is set to output 10 samples per second. This permits 100 ms of integration time per sample. This is sufficient to support both M_x and M_z operations at this output rate.

3. Test Results

The prototype magnetometer was initially tested in M_x mode with the sensor placed inside a solenoid located in a six-layer mu-metal shield to prevent the ambient magnetic field from penetrating the test environment and allowing precise control of the magnetic field strength and direction at the sensor. Following the discussion in section 2.1 to maximize the amplitude of the M_x modulation signal, the orientation of the sensor within the solenoid was chosen such that the angle between the solenoid center axis and the sensor optical axis was approximately 45°. With the VCSEL wavelength tuned to the D1 atomic transition, the Larmor frequency identifying the magnetic field strength is detected by searching for the resonance between the atomic spin precession and the RF magnetic field applied via the Helmholtz coils. Figure 6 shows the in-phase (Figure 6a) and quadrature (Figure 6b) components of the photocurrent as functions of the ambient magnetic field for three fixed RF frequencies between 37 kHz and 49 kHz. When the ambient magnetic field corresponds to the Larmor frequency of the RF field applied at these frequencies, the amplitude in the photocurrent assumes a minimum. Furthermore, the in-phase photocurrent vanishes, which is indicative of a phase shift between the applied RF magnetic field and the resonant response of 90°. These sensor responses represent the M_z and M_x effects, respectively. The field strength corresponding to the set resonant frequencies is identified as the zero crossing of the in-phase signal, which is observed to be 6499 nT, 7356 nT, and 8157 nT, respectively. The ratios of the differential resonance frequencies and magnetic field strengths yield a scale factor of 7 Hz/nT corresponding to the ^{87}Rb gyromagnetic ratio. An offset of 1166 nT is inferred in absence of a solenoid-generated magnetic field and is due to the residual background magnetic field. The jitter in the zero crossing of the in-phase signal gives an estimate of the combined variability due to solenoid field variations and instrument RMS noise, which amounts to about 0.1 nT. Since the solenoid power supply is only stable to 0.03%, or 0.3 nT, for a current of 1 mA, it is most likely that the origin of the observed variability is largely external to the instrument.

Once the resonance frequency is identified, it is tracked by a control loop implemented in the instrument's FPGA and the magnetic field magnitude is sampled at a cadence of 10 samples per second as described in section 2.3. The sensor response to different step-like changes in the magnetic field magnitude between 0.5 nT to 2 nT measured in M_x mode is illustrated in Figure 8. The sensitivity was derived from the noise in the photodiode signal, which contains all the sensor information and is processed by the FPGA to yield the lock-in estimates in data units. The variability in data units was converted to physical units using the scale factor obtained by fitting the linear slope of the in-phase error signal versus frequency near the resonance. As shown in Figure 6a, this slope is independent of the field magnitude. Conversion to magnetic field units is completed by applying the ^{87}Rb gyromagnetic ratio to the frequency values. Integration of a power spectrum

of the magnetic field magnitude over the 9.5 Hz bandwidth of the lock-in amplifier yielded an RMS variability of 44.6 pT. Assuming a flat spectrum over this narrow bandwidth, the sensitivity of the instrument is approximately 15 pT/√Hz. The measured closed loop noise variance is 50 pT to 60 pT RMS, which agrees reasonably well with the above spectral analysis. In addition to the applied test signals, the data shown in Figure 8 exhibit fluctuations on several timescales, which can have multiple origins, including the limited stability of the solenoid current, variable magnetic field sources within the building (e.g., moving metal doors and elevators), and instrumental drifts. The differentiation of these error sources is deferred to future work.

4. Conclusions

We have developed a low-resource, miniaturized, atomic scalar magnetometer based on the rubidium isotope ^{87}Rb suitable for operation in space. The design takes advantage of recent breakthroughs in microfabricated atomic devices and implements both M_x and M_z mode operation. The dual-mode operation combines the accuracy of M_z magnetometers with the higher sampling rates of M_x-based instruments. The measurements from the two modes were found to agree to better than one part in 10^{-3} in a 2000 nT applied field. Future work is required to investigate whether this level of agreement holds over a wider range of the ambient field. In M_x mode, a measured sensitivity of 15 pT/√Hz or about 0.1 nT RMS has been proven. The prototype instrument demonstrates substantial reductions of mass and power (500 g and 1 W, respectively) over conventional instruments and shows that atomic magnetometers can be miniaturized with acceptable performance to serve future planetary missions even under severe resource constraints.

Acknowledgments
This work was supported by the Johns Hopkins University Applied Physics Laboratory Internal Research and Development Program and by the National Aeronautics and Space Administration under grant agreement NNX14AK45G issued through the Science Mission Directorate. The data presented in the Figures 6–8 are included in the supporting information for this manuscript.

References

Acuña, M. H. (2002), Space-based magnetometers, *Rev. Sci. Instrum.*, *73*, 3717–3736.
Anderson, B. J., M. H. Acuña, D. A. Lohr, J. Scheifele, A. Raval, H. Korth, and J. A. Slavin (2007), The magnetometer instrument on MESSENGER, *Space Sci. Rev.*, *131*, 417–450.
Andreou, A. G. (2008), Silicon-on-sapphire CMOS and opportunities in niche markets: Old wine in a new bottle, *2008 IEEE International SOI Conference Proceedings*, pp. 9–12, doi:10.1109/Soi.2008.4656270.
Andreou, A. G., Z. K. Kalayjian, A. Apsel, P. O. Pouliquen, R. A. Athale, G. Simonis, and R. Reedy (2001), Silicon on sapphire CMOS for optoelectronic microsystems, *IEEE Trans. Circuits Syst.*, *1*, 22–30, doi:10.1109/7384.963464.
Back, E., and S. Goudsmit (1928), Kernmoment und Zeemaneffect von Wismut, *Z. Phys.*, *47*, 174.
Bloch, F. (1946), Nuclear induction, *Phys. Rev.*, *70*, 460–474.
Bloom, A. L. (1962), Principles of operation of the rubidium vapor magnetometer, *Appl. Opt.*, *1*, 61–68.
Colegrove, F. D., and P. A. Franken (1960), Optical pumping of helium in the S-3(1) metastable state, *Phys. Rev.*, *119*, 680–690.
Dougherty, M. K., et al. (2004), The Cassini magnetic field investigation, *Space Sci. Rev.*, *114*, 331–383.
Drung, D., C. Assmann, J. Beyer, A. Kirste, M. Peters, F. Ruede, and T. Schurig (2007), Highly sensitive and easy-to-use SQUID sensors, *IEEE Trans. Appl. Supercond.*, *17*, 699–704, doi:10.1109/Tasc.2007.897403.
Duret, D., J. Bonzom, M. Brochier, M. Frances, J. M. Leger, R. Odru, C. Salvi, T. Thomas, and A. Perret (1995), Overhauser magnetometer for the Danish Ørsted satellite, *IEEE Trans. Magn.*, *31*, 3197–3199.
Jaklevic, R. C., A. H. Silver, J. Lambe, and J. E. Mercereau (1964), Quantum interference effects in Josephson tunneling, *Phys. Rev. Lett.*, *12*, 159–160.
Knappe, S., V. Gerginov, P. D. D. Schwindt, V. Shah, H. G. Robinson, L. Hollberg, and J. Kitching (2005a), Atomic vapor cells for chip-scale atomic clocks with improved long-term frequency stability, *Opt. Lett.*, *30*, 2351–2353.
Knappe, S., P. D. D. Schwindt, V. Shah, L. Hollberg, J. Kitching, L. Liew, and J. Moreland (2005b), A chip-scale atomic clock based on Rb-87 with improved frequency stability, *Opt. Express*, *13*, 1249–1253.
Kominis, I. K., T. W. Kornack, J. C. Allred, and M. V. Romalis (2003), A subfemtotesla multichannel atomic magnetometer, *Nature*, *422*, 596–599.
Leger, J. M., F. Bertrand, T. Jager, M. Le Prado, I. Fratter, and J. C. Lalaurie (2009), Swarm absolute scalar and vector magnetometer based on helium 4 optical pumping, *Procedia Chem.*, *1*, 634–637, doi:10.1016/j.proche.2009.07.158.
Liew, L. A., S. Knappe, J. Moreland, H. Robinson, L. Hollberg, and J. Kitching (2004), Microfabricated alkali atom vapor cells, *Appl. Phys. Lett.*, *84*, 2694–2696.
Liew, L. A., J. Moreland, and V. Gerginov (2007), Wafer-level filling of microfabricated atomic vapor cells based on thin-film deposition and photolysis of cesium azide, *Appl. Phys. Lett.*, *90*, 114106, doi:10.1063/1.2712501.
Martin, M. N., and R. C. Meitzler (2012), A family of radiation tolerant ASICs for spacecraft monitoring and control operations, *2012 IEEE Aerospace Conference*, doi:10.1109/AERO.2012.6187236.
Marwick, M. A., F. Tejada, P. Pouliquen, E. Culurciello, K. Strohbehn, and A. G. Andreou (2006), Dark current and noise of 100 nm thick silicon on sapphire CMOS lateral PIN photodiodes, *2006 IEEE International Symposium on Circuits and Systems*, pp. 4583–4586, doi:10.1109/Iscas.2006.1693650.
Mhaskar, R., S. Knappe, and J. Kitching (2012), A low-power, high-sensitivity micromachined optical magnetometer, *Appl. Phys. Lett.*, *101*, 241105, doi:10.1063/1.4770361.
Podzolko, M. V., I. V. Getselev, Y. I. Gubar', and I. S. Veselovsky (2009), Radiation conditions of a mission to Jupiter and Europa, *Solar Syst. Res.*, *43*, 116–120, doi:10.1134/S0038094609020038.
Reigber, C., H. Luhr, and P. Schwintzer (2002), CHAMP mission status, *New Trends Space Geodes.*, *30*, 129–134.
Schwindt, P. D. D., S. Knappe, V. Shah, L. Hollberg, J. Kitching, L. A. Liew, and J. Moreland (2004), Chip-scale atomic magnetometer, *Appl. Phys. Lett.*, *85*, 6409–6411.

Schwindt, P. D. D., B. Lindseth, S. Knappe, V. Shah, J. Kitching, and L. A. Liew (2007), Chip-scale atomic magnetometer with improved sensitivity by use of the M_x technique, *Appl. Phys. Lett.*, *90*, 081102, doi:10.1063/1.2709532.

Shah, V., S. Knappe, P. D. D. Schwindt, and J. Kitching (2007), Subpicotesla atomic magnetometry with a microfabricated vapour cell, *Nat. Photonics*, *1*, 649–652, doi:10.1038/nphoton.2007.201.

Smith, C. W., J. L'Heureux, N. F. Ness, M. H. Acuña, L. F. Burlaga, and J. Scheifele (1998), The ACE magnetic fields experiment, *Space Sci. Rev.*, *86*, 613–632.

Smith, E. J., B. V. Connor, and G. T. Foster (1975), Measuring the magnetic fields of Jupiter and the outer solar system, *IEEE Trans. Magn.*, *11*, 962–980, doi:10.1109/Tmag.1975.1058779.

Tejada, F., A. G. Andreou, and P. O. Pouliquen (2006), Stacked, standing wave detectors in 3D SOI-CMOS, *2006 IEEE International Symposium on Circuits and Systems*, pp. 1315–1318, doi:10.1109/Iscas.2006.1692835.